PHYSICAL REVIEW D VOLUME 21, NUMBER 7 1 APRIL 1980

Measurement of radiative π^+p scattering below the $\Delta^{++}(1232)$ resonance

D. E. A. Smith, P. F. Glodis, R. P. Haddock, K. C. Leung, and M. A. Tamor

University of California, Los Angeles, California 90024

(Received 13 November 1979)

We report measurements of $\pi^+p \rightarrow \pi^+p\gamma$ at 17 photon angles for 165-MeV incident pions. Like the previously reported data for 269-, 298-, and 324-MeV incident pions, these data show little structure and do not deviate significantly from models predicting a monotonic decrease of the photon energy spectra with increasing photon energy.

I. INTRODUCTION

The $\pi p \rightarrow \pi p\gamma$ reaction is of theoretical interest as a source of information on the following subjects: (a) the range of validity of soft-photon theorems, (b) off-mass-shell πp scattering amplitudes, (c) model calculations such as effective-Lagrangian, static and potential models, PCAC (partial conservation of axial-vector current) and current-algebra calculations, and (d) the electromagnetic properties of πN resonances.

We report here a measurement of the $\pi^+p \rightarrow \pi^+p\gamma$ photon energy spectra for 17 photon angles at an incident π^+ energy of 165 MeV. The mean interaction energy is 161 MeV corresponding to a c.m. energy of $\sqrt{s} = 1210$ MeV. In previous experiments, we have reported measurements of $\pi^\pm p \rightarrow \pi^\pm p\gamma$ spectra at $\sqrt{s} = 1291$, 1309, and 1330 MeV.[1-4]

The chief characteristic of these data was reasonable agreement with a Low[5]-type soft-photon theorem for laboratory photon energies E_γ up to $\simeq 50-60$ MeV and a $1/E_\gamma$ falloff at higher photon energies.

These data were surprising in that they disagreed with effective-Lagrangian[6] and modified Low[7] calculations, both of which predicted a sizable bump in the photon spectrum for photons emitted in the backward direction. Such a bump was expected due to structure radiation from the virtual πp system. Specifically, a significant enhancement due to magnetic dipole radiation from the $\Delta^{++}(1232)$ was expected.

A number of theoretical investigations have attempted to explain the data. Corrections, criticisms, and improvements of the effective-Lagrangian model of Ref. 6 have been made by Vanzha and Musakhanov,[8] Beder,[9] and Musakhanov.[10] An interesting aspect of Ref. 10 is the incorporation of a partially conserved axial-vector current and current algebra to study the soft-pion limit of the $\pi^+p \rightarrow \pi^+p\gamma$ amplitude using data from neutrino-induced pion production. A value of $(3.6 \pm 2) \times$(total proton magnetic moment μ_p) was obtained for $\mu_{\Delta^{++}}$, the magnetic moment of the $\Delta^{++}(1232)$, as compared to $2\mu_p$ predicted by SU(6).[11] Improvements and corrections to the soft-photon theorem have also been made by Pascual and Tarrach,[12] and by Liou and Nutt.[13-15] Reference 12 uses a soft-photon theorem and an approach based on a narrow-width approximation for the Δ^{++} to calculate a bremsstrahlung cross section with only one free parameter $\mu_{\Delta^{++}}$. Comparing their results with previous UCLA bremsstrahlung data taken at $T_\pi = 298$ MeV, they find $\mu_{\Delta^{++}} = (2.0 \pm 0.8)\mu_p$ in good agreement with SU(6). Liou and Nutt use a soft-photon approximation which expands both kinematic and dynamic cross-section terms in E_γ. Their results are in good agreement with our previous data,[1-4] and they suggest that the contributions from off-mass-shell effects and resonances are small. Thompson[16] and Ho-Kim and Lavine[17] have considered static models, and Bosco *et al.*[18] and Ho-Kim and Lavine[19] have shown reasonable agreement with the data can be obtained from the Chew-Low static model with pion current and recoil nuclear effects included. Piccioto[20] has analyzed the $\pi^-p \rightarrow \pi^-p\gamma$ data to investigate off-mass-shell effects. In summary, corrections and modifications have been applied to theoretical models to yield a more or less monotonically decreasing photon spectrum without the bump expected due to the $\Delta^{++}(1232)$ and its structure radiation.

The present experiment is an extension of our investigation of π^+p radiative scattering to the region below the $\Delta^{++}(1232)$ resonance. In the previous work all the final-state particles were detected. The outgoing angle of each particle was measured along with the scattered pion momentum and, with less accuracy, the proton's residual range. The energy of the photon was not measured.

This information allowed a doubly overconstrained (2C) kinematic fit to the radiative hypothesis for each event. Events were selected on the basis of this fit in conjunction with the photon time-of-flight information. Target-empty runs showed that a negligible target-empty subtraction was required.

Production of neutral pions in which only one of the π^0-decay photons was detected constituted a possible source of false events. These events were rejected by using the pion and proton information to calculate a neutral-particle missing mass. The resolution was sufficient to give a clear separation between radiative photons and those originating in π^0 decay.

In the present experiment the lower incident pion energy does not permit detection of the recoil proton except for events originating in a thin region of the target nearest the proton detector. Therefore, the radiative events must be extracted from data based on a less restrictive trigger involving only the pion and photon. Using only this information, an exact solution to the radiative kinematic hypothesis can be constructed for each event. The final numbers of radiative events for each photon-energy interval are then determined by a liquid-hydrogen in-out subtraction, a cut which selects events from the hydrogen flask with correct photon time of flight and a subtraction to remove random photon time-of-flight background events in the in-time window.

Because the reconstructed radiative events are not overconstrained, the question of background rejection is very important. With this in mind, the incident beam energy was chosen below the threshold for π^0 production on hydrogen. Production of π^0's from carbon and aluminum in the target walls may still take place, but the scattered π^+ would not have sufficient energy to traverse the pion magnetic spectrometer.

The final energy of 165 MeV represents a compromise. Theoretical considerations, such as tests of πp potential models and comparison with soft-pion theorems, indicate a low incident energy, preferably under 100 MeV. Experimentally, however, this low an energy is undesirable because of an increased rate of pion decay and a large positron contamination.

In the following sections we describe the experimental apparatus, data-reduction procedures, and cross-section evaluation. We concentrate on the differences between the procedures here and those described in Refs. 2–4. In the final section a comparison of the data is made with some of the published theoretical predictions.

II. EXPERIMENTAL METHOD AND APPARATUS

Measuring the $\pi^+p \to \pi^+p\gamma$ cross section demands an apparatus with a very large acceptance. The experimental arrangement consisted of a wide-aperture magnetic pion spectrometer with spark chambers before and after the bending magnet and an array of lead-glass Cerenkov counters for photon detection. This apparatus was similar to that described in Ref. 4 except that the proton detection arm was not used in the radiative trigger. The proton detector was used in subsidiary elastic scattering measurements to confirm the beam energy.

The beam

Incoming pions were produced at 0° in the external proton beam of the Lawrence Berkeley Laboratory 184-in. Synchrocyclotron. The pion production target consisted of 33 cm of CH_2 (polyethylene) with 5 cm of lead upstream used as an energy degrader. The double-bend intermediate-focus pion beam had a 5.6-cm CH_2 degrader placed at the first focus to eliminate protons. The amounts of CH_2 and lead were chosen to attain maximum rate. About halfway through the data taking, the lead was removed and the CH_2 degrader reduced to 2.5 cm. The production target was not altered again. The beam parameters are given in Table I.

Target

The proton target (Fig. 1) was a flask of liquid hydrogen 6.73 cm wide with a 0.84-mm mylar wall. The long axis (Y_T) of the target was inclined at an angle of $20.5 \pm 0.5°$ to the beam line.

The average length of hydrogen traversed by an incoming beam particle was 19.2 ± 1.0 cm. The

TABLE I. Beam parameters.

Laboratory momentum[a,b] (MeV/c)	Kinetic energy[a,b] (MeV)	Momentum spread[c]	Muon/pion ratio[c]	e^+/beam ratio[d]	Average $\sec^{-1}$
271 ± 3	165.5 ± 2.5	±1%	0.10 ± 0.05	0.20 ± 0.10	5.3×10^5

[a] Just before entering target vacuum chamber.

[b] Determined from range in copper, corrected for multiple scattering, and checked by reconstruction from elastic events with proton information.

[c] Calculated from differential range curve.

[d] Extrapolated from our measurements at higher energies.

liquid hydrogen was in equilibrium with hydrogen gas in a closed system at slightly less than atmospheric pressure. The target flask was surrounded by a gas ballast flask with 0.25-mm mylar walls and 20 layers of 0.006-mm aluminized mylar superinsulation. The vacuum chamber surrounding the gas ballast was a 17.8-cm diameter aluminum cylinder with 1.25-mm walls.

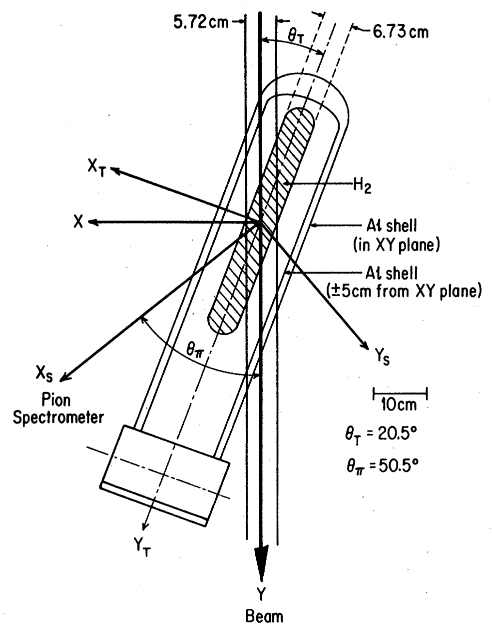

FIG. 1. Top view of the target. Axes and dimensions are as shown. The liquid-hydrogen density was 0.0708 g/cm^3. The mylar ballast flask is not shown.

TABLE II. Particle-detector locations. α is measured clockwise from the beam line in the horizontal plane and β is the angle of elevation measured upward from the horizontal plane. R is the distance from the target center. $\Delta\Omega_\gamma$ is the solid angle subtended by the counter viewed from the target center.

	α	β	R^a (cm)	$\Delta\Omega_\gamma$ (msr)
$G1$	−160°	0°	61.0	27.6
2	−160°	−18°	55.9	32.8
3	−160°	−36°	55.9	32.8
4	−140°	0°	55.9	32.8
5	−140°	−18°	55.9	32.8
6	−140°	−36°	55.9	32.8
7	−120°	0°	55.9	32.8
8	−120°	−18°	55.9	32.8
9	−120°	−36°	55.9	32.8
10	180°	−36°	55.9	32.8
11	160°	0°	63.5	25.4
12	140°	0°	63.5	25.4
13	120°	0°	63.5	25.4
14	105°	0°	63.5	25.4
15	105°	−20°	63.5	25.4
18	−40°	−56°	63.5	25.4
19	0°	−59°	63.5	25.4
pion	$(50.5\pm7.0)^{\circ\,b}$	$(0^{+24}_{-10})^{\circ\,b}$	73.8^c	

[a] Angles and distances measured to center of photon-counter face.

[b] Approximate angular acceptance.

[c] Distance to first-pion spark chamber.

The pion detector

The magnet employed was a "picture-frame" dipole with an aperture 183 cm by 46 cm, with a 46-cm gap between the pole faces. The magnet was oriented with the main component of the field horizontal, deflecting the π^+ downward. 5.7-cm iron plates were attached to both faces of the magnet to reduce the fringe field in the region of the spark chambers.

The trajectory of the outgoing pion was determined before the magnet by three wire spark chambers (50×75 cm, 75×75 cm, and 100×100 cm) with magnetostrictive readout. After the magnet the trajectory was determined by three 1×2 m magnetostrictive spark chambers. Four contiguous 63×46×1.3 cm scintillation counters ($\pi_1-\pi_4$) mounted behind the last spark chamber were used as part of the trigger and for time-of-flight determinations.

Photon detector

The photon detector consisted of 17 separate lead-glass Cerenkov counters (called G_1-G_{15}, G_{18}, G_{19}), whose positions are given in Table II. Details on the construction and calibration of the counters may be found in Refs. 2 and 21. The photon counters provided directional photon information as well as a timing signal for the photon time-of-flight determination.

Other counters

The incident beam was defined at the exit of the last quadrupole magnet by two scintillation hodoscopes. These consisted of four vertical counters ($V_1 - V_4$), each 1.9 cm wide, and six horizontal counters (H_1-H_6), each 2.5 cm wide. The beam was further defined just before the target by a 7.6×7.6×0.64 cm scintillator T, which was also used for timing and coincidence information.

An anticounter with a central hole, A_h, reduced accidental counts due to beam halo. The photon counters were guarded by anticounters A_g preventing spurious triggers by charged particles.

Fast electronics

An incident-beam pion was defined in the fast logic as

$$\pi_{\text{in}} = V_i H_j T C \bar{A}_h (\bar{V}_m + \bar{H}_m) .$$

Here C is a fast-timing signal from the cyclotron rf system used to reduce non-beam-related accidentals. $(\bar{V}_m + \bar{H}_m)$ represents the absence of multiple triggers in the beam hodoscopes.

A radiative event was defined as $E_{\text{rad}} = \pi_{\text{in}} G \pi_{\text{out}} \bar{A}_G$, where G represents a hit in a photon detector and π_{out} represents a signal from one of the four scintillation counters ($\pi_1 - \pi_4$) in the pion detector. $\bar{A}_G$ is the nontriggering of the associated photon anticounter.

Data collection

An on-line PDP-8/I computer handled all relevant data for each event. These data included the spark-chamber signals, counter latches, times of flight of outgoing particles, and photon-pulse height. Raw data were written onto magnetic tape for off-line analysis.

Data reduction

The following sequence of tests was applied to select candidates for radiative events. The percentages are fractions of the remaining events eliminated at each step.

(1) Fast-logic inefficiencies consisting of events with multiple or missing beam-hodoscope latches (11%) and events with multiple photon latches (2.6%) were eliminated.

(2) Events with insufficient sparks to reconstruct pion tracks were rejected (25%) and events with pion tracks missing the target aperture (28%) were rejected.

(3) The horizontal opening angle between the pion track at the entrance and exit of the magnet could not be greater than about 0.1 rad (22%). The exact cut was a function of pion momentum and calculated fringe-field effects. The distance between the points where the projected entrance and exit tracks appear to intercept the magnet midplane could not be more than 7.5 cm (8%).

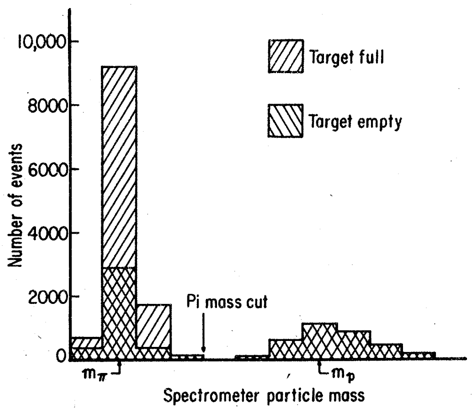

FIG. 2. Mass distribution of particles in the spectrometer calculated from pion time of flight and momentum. The pion-mass cut was placed as shown before any geometry cuts. The match between numbers of full and empty protons indicates the protons originate in the target walls.

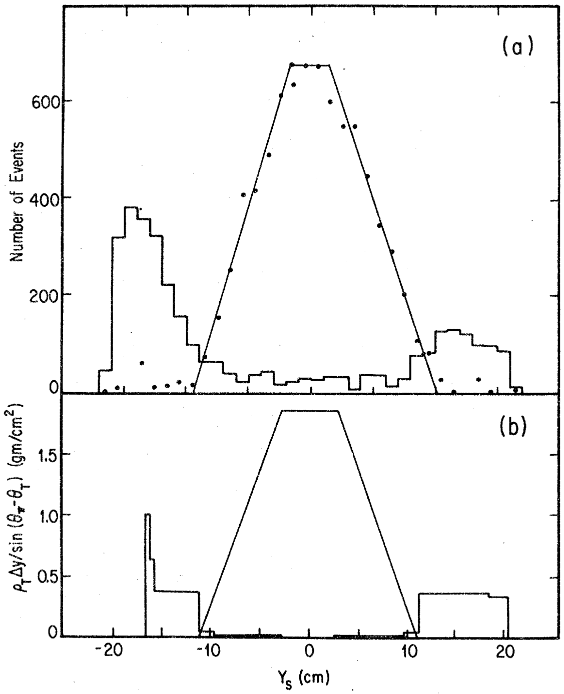

FIG. 3. (a) Distribution of events projected parallel to X_s onto Y_s (see Fig. 1). Histogram shows target-empty events normalized to the number of pions incident on the full target. Points are for the net (full-empty) distribution. Both distributions are cut on the calculated pion mass (see Fig. 2). Lines are a least-squares fit to the points. A cut was made on Y_s (-9.65 cm $< Y_s < 10.16$ cm). 1.6% of the net and 77% of the target-empty events lie outside the cut. (b) Relative mass distribution of the target as viewed at $Z = \pm 5$ cm projected parallel to X_s onto Y_s. The pion beam was assumed to be 5.7 cm wide. The mass distribution does not reflect the dependence of the photon counter solid angle on the interaction point or the relative photon production probabilities of aluminum and hydrogen.

Events surviving these cuts were written on a summary tape for further analysis. The summarized events were treated as follows:

(1) The momentum of the outgoing π^+ was calculated using the vertical bend between the tracks. This momentum and the outgoing-pion time of flight were used to calculate m_π (Fig. 2). Rejecting all events with $m_\pi > 400$ MeV/c^2 eliminated protons in the spectrometer. This removed 48% of the target-empty events and 23% of the target-full events.

(2) A difficult point in the analysis was the correct selection of target cuts. The incoming pion was assumed to have passed through the center of the latched vertical hodoscope counter and the center of the beam counter T. The outgoing pion line was taken as the extension of the spark-chamber track. The event vertex was then taken as the intersection of the outgoing pion line and a vertical plane including the incoming pion line.

A cut on the vertical target coordinate eliminated events appearing to originate more than 5 cm above or below the target median plane, a region not directly illuminated by the beam.

A cut was made on the target interaction point to eliminate events from the target walls. Figure 3(a) shows the distribution of event vertices projected on a plane through the target center normal to the magnet axis. The vertex distribution of the target-empty events is easily understood from the target-mass distribution shown in Fig. 3(b). Both distributions show clear peaks where the target walls are located. Vertex cuts at −9.65 and 10.16 cm along the Y_s axis eliminate 77% of the target-empty events and 24% of the target-full events, leaving a small target-empty background to be subtracted away. During the empty-target runs a small amount of gaseous helium was present in the target flask and, to minimize the effect of this in the empty-target background subtraction, the target cut on the empty runs excluded the central 7.6 cm along Y_s. We found that events which originated in the target walls and the aluminum can were much more likely to be associated with an in-time photon than events in which the interaction occurred in liquid hydrogen. We believe this is consistent with the reasonable hypothesis that pions are more likely to radiate when scattering from heavier nuclei. The target cuts we have chosen, along with the empty-target background subtraction, seem to have effectively eliminated contamination of our E_γ spectra by these target-wall events.

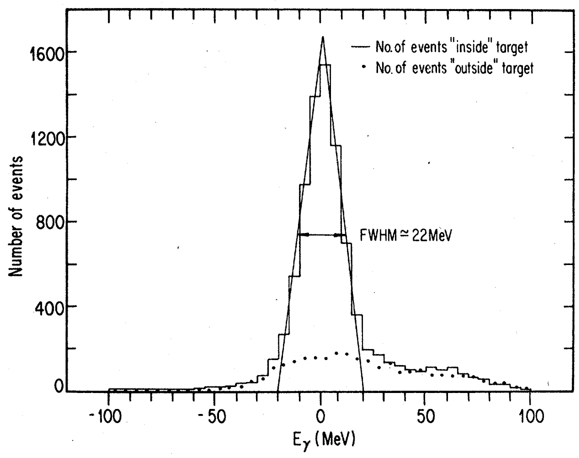

FIG. 4. Photon energy spectrum of all events passing geometry cuts (histogram). Lines are a least-squares fit to the histogram. Points are the spectrum of events lying outside the target. No photon time-of-flight cuts have been imposed.

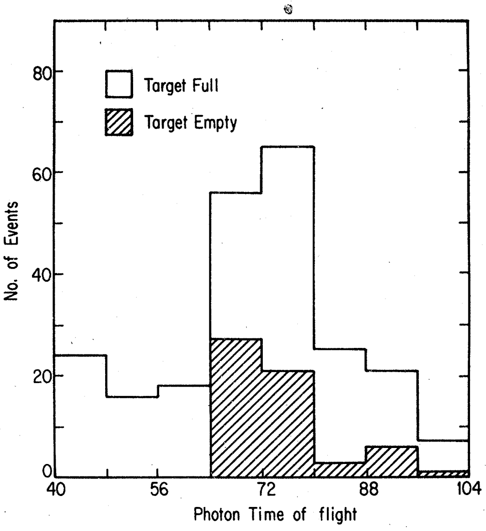

FIG. 5. Photon time-of-flight distributions (approximately 0.3 ns per channel) for photon counters 1, 2, 5, and 7 combined for a group of target-full runs and for a group of appropriately normalized target-empty runs. Events with calculated photon energies below 15 MeV were excluded.

(3) The photon energy was reconstructed kinematically using the incoming and outgoing pion momenta and the photon angle. With the target-empty events subtracted away, this yields a photon energy spectrum (Fig. 4) peaked at about 2 MeV. The spectrum agrees with expectations in two ways. First, the spectrum decreases asymptotically to zero in the $E_\gamma < 0$ region, indicating that all non-π^+p events have been removed. Second, there is a dominating peak at $E_\gamma \simeq 0$. This peak is attributed to elastic events in coincidence with a random photon trigger. These elastic events, analyzed as radiatives, should all reconstruct with exactly zero photon energy. The width of the elastic peak, ~22 MeV, reflects the resolution of the photon-energy reconstruction. This resolution, ±11 MeV, is to be compared with ±3.5 MeV in previous experiments in which the outgoing proton was detected.

(4) A photon time-of-flight spectrum, after subtraction of the appropriately normalized target-empty events, consists of a radiative peak on a random-time background. The background is eliminated by a photon time-of-flight cut about the radiative signal followed by a subtraction to correct for random events inside the time-of-

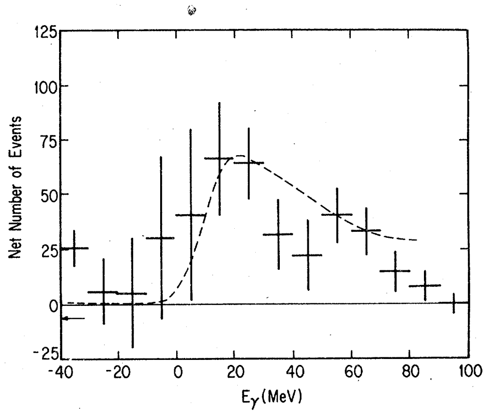

FIG. 6. Net photon energy spectrum. The crosses represent the number of events after photon time-of-flight background and empty-target subtractions. Errors are purely statistical. The dotted line is a Monte Carlo simulation based on the assumption that the number of events will be proportional to $1/E_\gamma$. This idealized cross section has been corrected for the efficiency of the photon counters and for the effects of π-μ decay, but the curve cannot be expected to agree well with the data beyond 20 MeV since the effects of detector solid angles, absorptions, and efficiencies have been ignored above that energy. In addition, the $1/E_\gamma$ assumption for the cross section is simplistic. The arrow on the left side of the figure denotes the total number of events between −40 and −120 MeV: -6.2 ± 7.5.

flight cut. A typical photon time-of-flight spectrum for a group of counters is shown in Fig. 5.

(5) The photon energy spectrum after the time-of-flight subtractions is shown in Fig. 6. For $E_\gamma \lesssim -20$ MeV, the spectrum has few net events and, except for one bin, is statistically consistent with zero. The rise as E_γ increases from 0 to 20 MeV is due to the increasing photon counter efficiency. The negative-energy tail is a reflection of the photon energy resolution discussed earlier. Comparing Figs. 4 and 6 in the E_γ region near zero shows that the photon time-of-flight cut and background subtraction have effectively removed random elastic events. Also shown in Fig. 6 is a simulated photon energy spectrum which is obtained by folding a Gaussian of $\sigma = 11$ MeV through a theoretical spectrum weighted by photon counter efficiency. The distortion of the E_γ spectrum from mismeasurement of the outgoing pion track due to $\pi\to\mu\bar{\nu}$ decays is also included in the curve. In spite of the simplicity of the theoretical model and the deliberate omission of several known experimental effects, the curve seems to characterize well the shape of the data as a function of E_γ.

The most serious problem in the analysis of the data was the effect on the reconstructed photon energy of the scattered pion decaying. This was studied by analyzing Monte Carlo-simulated $\pi\to\mu\bar{\nu}$ decays. The Monto Carlo program simulated the effects of multiple scattering, the phase space of the beam, and the geometry and resolution of the detectors. Pion and muon trajectories were numerically stepped through the pion spectrometer using a map of the actual magnetic field. It was found that Monte Carlo-generated pion decays tended to produce E_γ spectra with a substantial bump at about 60 MeV. This bump was not seen in the E_γ spectra generated without decays. In the actual data, this enhancement could be seen by looking at events which appeared to originate above and below the volume of the target accessible to the beam. The interaction points of these events were presumably miscalculated because the outgoing pion decayed in flight, putting a "kink" in the track before it reached the first set of pion spark chambers. Based on the Monte Carlo results, a correction was applied to the photon-energy spectra which had the effect of changing the photon-energy assignments of a small number of events.

Cross-section calculation

The differential cross section was calculated in the laboratory frame for each photon counter i and photon-energy interval $E_\gamma \pm \frac{1}{2}\Delta E_\gamma$ as

$$d\sigma_i(E_\gamma) = \frac{d^5\sigma_i}{d\Omega_\pi d\Omega_\gamma dE_\gamma} = \frac{Y_i}{BT\Delta E_\gamma(\Delta\Omega_\pi)_i(\Delta\Omega_\gamma\epsilon_\gamma)_i\epsilon_{sc}\epsilon_c\epsilon_{surv}}\,.$$

Y_i = net number of events after all subtractions with photon energy in the interval $E_\gamma \pm \frac{1}{2}\Delta E_\gamma$. This number has been corrected for the effects of $\pi\to\mu\bar{\nu}$ decay. The correction, calculated by Monte Carlo simulation of π decays, in most cases alters the uncorrected value of Y_i by less than 10%.

B = number of incident pions given by

$$B = N_B(1-\eta_e)(1-\eta_\mu)(1-\eta_{\text{mult}}) \times(1-\eta_{\text{att}})(1-\eta_{\text{anti}})(1-\eta_{\gamma d})\,,$$

where N_B is the recorded number of incident pions, and the factors are η_e = fractional electron contamination, η_μ = fractional muon contamination, η_{mult} = probability of multiple beam particles within resolving time causing rejection by the analysis program, η_{att} = attenuation of beam pions enroute to average interaction point, η_{anti} = fraction of events rejected by random γ-anticounter triggers, $\eta_{\gamma d}$ = fraction of events rejected due to multiple γ-counter latches.

T = number of target protons per unit area transverse to the beam.

ΔE_γ = width of photon-energy interval.

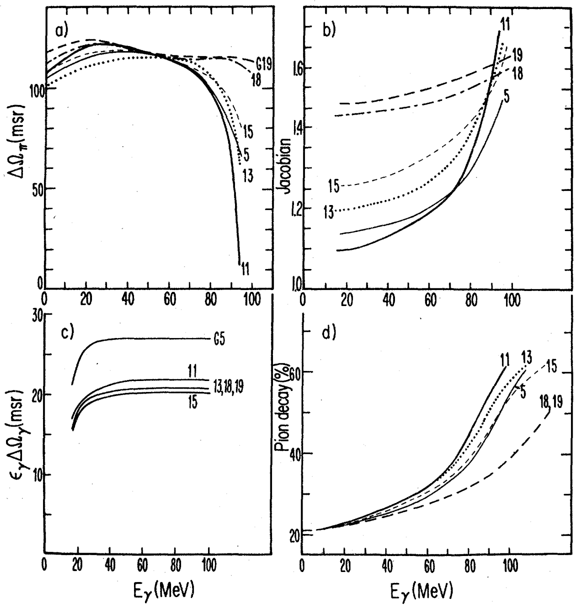

FIG. 7. Monte Carlo–calculated photon energy- and counter-dependent cross-section factors as described in the text.

$(\Delta\Omega_\pi)_i$ = effective solid-angle acceptance for pions, calculated by Monte Carlo event simulation [Fig. 7(a)].

$(\Delta\Omega_\gamma\epsilon_\gamma)_i$ = effective solid angle, weighted for efficiency of photon counter i [Fig. 7(c)], determined by Monte Carlo.

ϵ_{sc} = spark-chamber efficiency, calculated from the relative number of two- and three-spark fits.

ϵ_c = efficiency of scintillation counters.

ϵ_{surv} = photon-energy-dependent probability of survival of the outgoing pion and photon = $(1-\eta_\gamma)(1-\eta_\pi)[1-\eta_d(1-\eta_{rd})]$. The correction factors are η_γ = probability of photon loss in the target or anticounters, η_π = attenuation of outgoing pions, η_d = probability of pion decay [Fig. 7(d)], η_{rd} = probability of acceptance for a decayed event (η_d, η_{rd} calculated by Monte Carlo simulation).

Numerical values for all non-γ-counter-dependent cross-section factors are given in Table III. The γ-counter-dependent factors are shown for sample counters in Figs. 7(a)–7(d).

Table IV gives the cross section in the laboratory system for each photon counter and energy interval, and Fig. 7(b) shows the Jacobian factor $J = d\Omega_\pi^* d\Omega_\gamma^* dE_\gamma^* / d\Omega_\pi d\Omega_\gamma dE_\gamma$ to convert the cross section to the center-of-mass system.

III. RESULTS

The laboratory differential cross sections $d^5\sigma/d\Omega_\pi d\Omega_\gamma dE_\gamma$ for the 17 photon counters are given in Table IV. Large photon time-of-flight and empty-target background subtractions produce large statistical errors in the measured cross sections and, in cases where the cross sections are small, some unphysical negative results are found. To facilitate integrating our cross sections over photon energies or photon counters and to prevent biasing the results towards larger values of $d^5\sigma$, these negative results are not suppressed in Table IV.

TABLE III. Normalization factors and corrections used in cross-section calculation. The symbols are defined in the text. ϵ's designate absolute efficiency factors. The η's are percent corrections which reduce the effective number of beam particles.

Factor or correction	E_γ-independent factors Target full	Target empty
T	$7.62 \pm 0.4 \times 10^{23}$	not applicable
N_{beam}	3.25×10^{10}	1.08×10^{10}
ϵ_{sc}	0.85 ± 0.03	0.83 ± 0.3
ϵ_c	0.98 ± 0.01	same as full
η_{multi}	$(7.43 \pm 2)\%$	same as full
η_{att}	$(4.8\ \pm 1)\%$	not applicable
η_{anti}	$(4.16 \pm 2)\%$	same as full
$\eta_{\gamma d}$	$(2.6\ \pm 0.5)\%$	same as full

E_γ-dependent corrections

Corr \ E_γ(MeV)	17.5	25	35	45	55	65	75	85	95
η_π	6.0%	4.4%	3.6%	2.6%	1.9%	1.3%	0.7%	0.3%	0%
η_{rd}	0.34	0.35	0.37	0.40	0.43	0.48	0.57	0.65	0.7

TABLE IV. Individual photon-counter cross sections. The photon energies listed in the table represent the center of 10-MeV-wide photon-energy bins, except for 17.5-MeV data which correspond to $15 < E_\gamma < 20$ MeV.

Photon energy (MeV)	17.5	25	35	45	55	65	75	85	95
*G*1	22.2 ± 23.5	−1.3 ± 8.9	14.2 ± 9.3	−15.5 ± 20.5	0.1 ± 6.4	14.5 ± 7.2	−3.0 ± 2.3	−3.2 ± 2.8	
2	21.3 ± 18.7	8.4 ± 7.9	−16.4 ± 16.0	2.0 ± 16.6	3.4 ± 12.2	−1.3 ± 12.4	6.1 ± 6.3	3.7 ± 3.9	−9.8 ± 8.0
3	−31.8 ± 28.9	12.1 ± 14.0	19.8 ± 9.4	6.6 ± 5.8	−5.5 ± 10.8	23.8 ± 9.4	6.3 ± 4.9	−1.2 ± 13.3	
4	17.6 ± 27.5	10.5 ± 9.2	6.8 ± 7.2	7.0 ± 7.2	3.7 ± 11.9	11.2 ± 8.1	3.1 ± 3.5		
5	−4.9 ± 23.4	13.1 ± 10.1	5.1 ± 6.2	10.9 ± 7.0	−1.2 ± 4.0	0.7 ± 7.7	13.2 ± 7.8	0.4 ± 4.4	5.7 ± 6.8
6	−29.9 ± 35.6	14.5 ± 10.1	−16.0 ± 10.9	5.3 ± 5.9	4.1 ± 4.8	8.2 ± 6.2	−1.1 ± 7.9		
7	25.3 ± 32.6	18.2 ± 11.8	−16.0 ± 14.8	9.5 ± 6.8	3.9 ± 11.6	0.2 ± 8.5	−2.6 ± 11.2	19.1 ± 10.4	
8	67.2 ± 28.8	16.5 ± 10.4	10.8 ± 14.0	0.5 ± 10.4	10.9 ± 5.9	1.7 ± 5.2	−0.5 ± 5.7	14.8 ± 7.3	−14.2 ± 12.9
9	−12.3 ± 28.1	3.4 ± 13.7	13.0 ± 9.8	9.5 ± 11.7	15.7 ± 7.4	13.9 ± 7.5	−3.2 ± 10.8	7.6 ± 5.5	0.9 ± 5.0
10	−1.8 ± 23.2	15.9 ± 15.6	1.0 ± 12.5	14.5 ± 7.9	−9.4 ± 10.9	3.4 ± 6.1	6.7 ± 4.6		
11	−2.0 ± 22.1	7.7 ± 9.5	0.8 ± 8.7	−21.7 ± 16.4	43.1 ± 14.3	1.7 ± 6.4	3.6 ± 4.2		
12	39.8 ± 23.0	10.7 ± 14.4	5.8 ± 15.3	13.5 ± 9.1	5.9 ± 7.4	13.6 ± 11.7	0.9 ± 5.4		34.0 ± 36.5
13	76.8 ± 47	22.9 ± 20.1	28.3 ± 19.6	17.3 ± 10.7	25.8 ± 13.4	−9.5 ± 18.5	4.3 ± 4.6	−4.1 ± 3.2	
14	134.2 ± 51	−11.0 ± 21.7	4.8 ± 16.8	−3.8 ± 15.2	10.4 ± 12.0	−5.7 ± 9.5	−12.5 ± 15.2	−3.5 ± 3.2	−5.1 ± 4.6
15	103.6 ± 42	79.9 ± 23.4	9.8 ± 12.2	14.3 ± 20.8	−2.4 ± 15.2	23.1 ± 13.2	12.7 ± 10.2	−17.3 ± 15.7	
18	31.3 ± 47	13.0 ± 18.9	30.5 ± 18.2	−16.7 ± 22.5	32.7 ± 12.5	7.5 ± 7.3	14.3 ± 9.7	−4.0 ± 6.2	6.5 ± 9.4
19	78.6 ± 57	30.6 ± 27.5	46.3 ± 18.4	49.4 ± 16.5	6.6 ± 12.1	28.4 ± 12.1	5.7 ± 17.1	−5.0 ± 16.8	3.5 ± 16.4
*G*1–10	7.0 ± 8.7	11.3 ± 4.1	2.0 ± 3.6	5.4 ± 3.5	2.6 ± 2.9	7.5 ± 2.9	2.6 ± 2.3	4.2 ± 2.1	−1.8 ± 1.7
11, 12, 13, 15	54.5 ± 19.2	30.3 ± 9.6	11.2 ± 7.5	5.9 ± 7.4	18.1 ± 6.7	7.2 ± 6.6	5.4 ± 3.4	−5.3 ± 4.0	8.5 ± 8.9
18, 19	55.0 ± 38	21.8 ± 16.9	38.4 ± 13.8	16.3 ± 13.5	19.6 ± 9.0	18.0 ± 7.3	10.0 ± 9.9	−4.5 ± 8.9	5.0 ± 9.5
All counters	28.0 ± 9.2	15.1 ± 4.3	7.7 ± 3.4	6.1 ± 3.2	7.9 ± 3.0	7.9 ± 2.7	3.1 ± 2.1	1.0 ± 1.8	0.8 ± 2.3

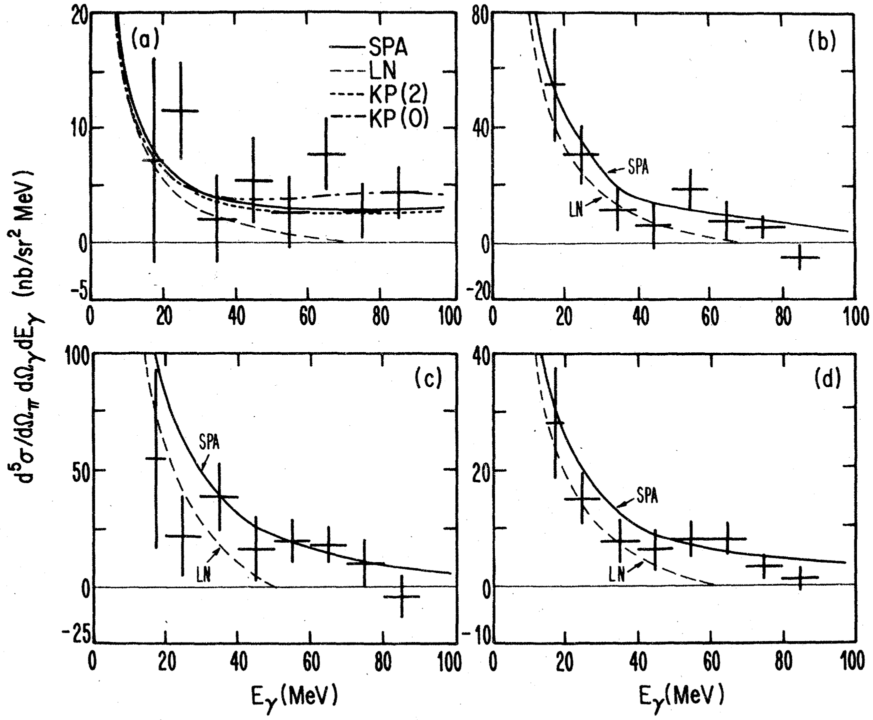

FIG. 8. Cross sections averaged over groups of counters. Curves shown in (a)–(d) are SPA and the calculation of Liou and Nutt (Ref. 22). (a) also shows the Lagrangian-model calculation of Kondratyuk and Ponomarev for $\mu_{\Delta^{++}} = 2\mu_p$ and $\mu_{\Delta^{++}} = 0$.

The measured differential cross sections for four groups of photon counters are shown in Figs. 8(a)–8(d), plotted against photon energy. Shown for comparison are two theoretical calculations based on the Low theorem[2,13,14,22] and [in Fig. 8(a)] the results of an effective-Lagrangian model calculation[6] for two different values of the Δ^{++} magnetic dipole moment.

All of the theoretical cross sections displayed in Fig. 8 have been calculated for a "point" geometry, with the outgoing pion following the axis of the spectrometer at 50.5° to the beam. The large acceptance of the pion spectrometer, approximately 120 msr, permitted the detection of events which were rather far from the point geometry. The horizontal component of the angle of the scattered pion with respect to the beam varied from 44 to 59°. The angle the scattered pion made with the horizontal plane is fairly uniformly distributed between 10° below the plane and 22° above it. The asymmetry is due to the vertical bend used in the pion spectrometer. For these reasons, the only reliable method for making counter-by-counter comparisons of theory with data is to use a Monte Carlo program to average the theoretical predictions over the acceptance of the detectors. To aid in this, a table of ratios between point geometry and Monte Carlo–averaged soft-photon-approximation (SPA) calculations is available from the authors.

For comparison of data with theoretical predictions averaged over groups of photon counters, performance of an average over the pion-detector acceptance is less important. The theoretical cross section for each counter group shown in Fig. 8 is taken as the γ-counter solid-angle weighted average of the cross sections for each counter of the group. The scattered pion direction was taken as lying in the horizontal plane along the "coplanar central ray" to the magnet rather than as the actual average pion direction because the difference in results was small and several calculations have appeared in the literature using the "central ray" geometry.

The soft-photon approximation, shown in Fig. 8, is based on the Low theorem and is described in Ref. 2. This calculation, applied to our previous results at beam energies of 260 MeV and above, substantially overestimated the cross sections for photon energies greater than 40 MeV. This effect does not occur at our 165-MeV beam energy, and the SPA calculation is in reasonable agreement with the data at all photon energies.

Another variation on the Low theorem is the calculation by Liou and Nutt.[13,14,22] They take the direction of the outgoing pion as defining an elastic event about which they expand in E_γ all kinematic and dynamic factors. Their cross section has the form

$$\sigma = (\sigma_{-1}/E_\gamma) + \sigma_0 \,,$$

where

$$\sigma_{-1} = \lim_{E_\gamma \to 0} (E_\gamma \sigma) \,,$$

$$\sigma_0 = \lim_{E_\gamma \to 0} \frac{\partial}{\partial E_\gamma} (E_\gamma \sigma) \,.$$

Their model has given the best agreement so far with our previously published $\pi^+ p \to \pi^+ p \gamma$ cross sections and their agreement with the present data is fair. However, for photon energies greater than about 60 MeV, their predicted cross sections become negative in all counters. This defect was much less severe at the higher beam energies of our previous experiments. Liou and Nutt suggest that the contribution from the sum of higher-order terms in E_γ, $\sigma_1 E_\gamma + \sigma_2 E_\gamma{}^2 + \cdots$, must be positive and large enough so that the final cross section will be positive when all contributions are included.

The results of an effective-Lagrangian-model calculation by Kondratyuk and Ponomarev,[6] hereafter KP, are shown in Fig. 8(a) for two different values of the Δ^{++} magnetic dipole moment $\mu_{\Delta^{++}}$. At this beam energy the predicted dependence of the E_γ spectrum on $\mu_{\Delta^{++}}$ is slight. At higher beam energies the KP calculation predicts a large bump at $E_\gamma \approx 100$ MeV in the cross section for photons in the backward direction (around $\alpha = -140°$). This sensitivity of the cross section to the value of $\mu_{\Delta^{++}}$ was one of the original motivations of the experiments described in Refs. 1–4. These measurements found monotonically decreasing cross sections with no evidence of the predicted structure.

The data from this experiment also show the same behavior with increasing photon energy. In contrast to the theoretical situation at higher beam energies, all the theoretical calculations discussed here behave in a roughly similar manner. All three are in fair agreement with experimental cross sections.

ACKNOWLEDGMENTS

We gratefully acknowledge the hospitality extended to us at the Lawrence Berkeley Laboratory and the assistance of Leal Kanstein and the crew of the 184-in. cyclotron. We wish to thank Mr. J. Hartlove and Mr. S. Jarrett for their assistance in taking data, and Mr. D. DeMars, Mr. M. O'Neill, and the late Mr. M. Thimel for their significant contributions to the data analysis. This work was supported in part by the Department of Energy, Contract No. DOE-EY-76-03-0010-PA25.

---

[1] M. Arman, D. Blasberg, R. Haddock, K. Leung, B. Nefkens, B. Schrock, D. Sober, and J. Sperinde, Phys. Rev. Lett. 29, 962 (1972).

[2] D. Sober, M. Arman, D. Blasberg, R. Haddock, K. Leung, B. Nefkens, B. Schrock, and J. Sperinde, Phys. Rev. D 11, 1017 (1975).

[3] K. C. Leung, M. Arman, H. C. Ballagh, Jr., P. F. Glodis, R. P. Haddock, B. M. K. Nefkens, and D. I. Sober, Phys. Rev. D 14, 698 (1976).

[4] B. M. K. Nefkens, M. Arman, H. C. Ballagh, Jr., P. F. Glodis, R. P. Haddock, K. C. Leung, D. E. A. Smith, and D. I. Sober, Phys. Rev. D 18, 3911 (1978).

[5] F. E. Low, Phys. Rev. 110, 974 (1958). Low's cases, *a* and *b*, with the appropriate form of the πp scattering amplitude are used to calculate the radiative amplitude. The five-dimensional differential cross section $d^5\sigma/dE_\gamma d\Omega_\gamma d\Omega_\pi$ ($d\Omega_\gamma$ and $d\Omega_\pi$ are the photon and pion solid angles, respectively) is computed by taking the usual sums and averages of spin states with a transverse radiation gauge.

[6] L. A. Kontratyuk and L. A. Ponomarev, Yad. Fiz. 7, 111 (1968) [Sov. J. Nucl. Phys. 7, 82 (1968)].

[7] W. E. Fischer and P. Minkowski, Nucl. Phys. B36, 519 (1972). A proposed modification of Low's soft-photon theorem to the case of radiative scattering near a resonance.

[8] A. P. Vanzha and M. M. Musakhanov, Dubna Report No. JINR-P2-6305, 1972 (unpublished).

[9] D. Beder, Nucl. Phys. B84, 362 (1975).

[10] M. M. Musakhanov, Yad. Fiz. 19, 630 (1974) [Sov. J. Nucl. Phys. 19, 319 (1974)].

[11] B. T. Feld, *Models of Elementary Particles* (Blaisdell, Waltham, Mass., 1969), Chap. 15.

[12] P. Pascual and R. Tarrach, Nucl. Phys. B134, 133 (1978).

[13] M. K. Liou and W. T. Nutt, Phys. Rev. D 16, 2176 (1977).

[14] M. K. Liou and W. T. Nutt, Nuovo Cimento 46A, 365 (1978).

[15] M. K. Liou, Phys. Rev. D 18, 3390 (1978).

[16] R. H. Thompson, Nuovo Cimento 16A, 290 (1973).

[17] Q. Ho-Kim and L. P. Lavine, Phys. Lett. 60B, 269 (1976); in *Meson-Nuclear Physics—1976*, proceedings of the International Topical Conference, Pittsburgh, edited by P. D. Barnes, R. A. Eisenstein, and L. S. Kisslinger (AIP, New York, 1976); Report No. COO-2171-58 (unpublished).

[18] B. Bosco, A. Conti, G. Landi, and F. Matera, Phys. Lett. 60B, 47 (1975).

[19] Q. Ho-Kim and J. P. Lavine, Report No. COO-2171-57 (unpublished).

[20] Ch. Picciotto, Nucl. Phys. A29, 41 (1975).

[21] D. I. Sober, M. Arman, D. J. Blasberg, R. P. Haddock, B. M. K. Nefkens, and K. C. Leung, Nucl. Instrum. Methods 108, 573 (1975).

[22] The calculations denoted SPA, Kondratyuk and Ponomarev, and Liou and Nutt have been carried out by us, using the formalisms presented in Refs. 2, 6, and 13,

respectively. Our versions of SPA and Liou and Nutt calculations have used the CERN-Kirsopp phase shifts [UCRL Report No. 20030 πN, 1970 (unpublished)] as input for the elastic scattering amplitudes. Our calculation of the cross section of Liou and Nutt disagrees somewhat with the author's own. We believe the discrepancy is due only to different choices of πp elastic phase shifts. Liou and Nutt have informed us that their calculation of their cross section is in better agreement with the data than the calculation shown here.